Structural, spectroscopic, luminescence and magnetic properties of a novel far-red emitting phosphor Er, Mn doped ZrTe3O8

S. Kabadou, J. Horcheni, F. Mselmi, A. Kabadou, E. Dhahri, Lotfi Bessais

Structural, spectroscopic, luminescence and magnetic properties of a novel far-red emitting phosphor Er, Mn doped $ZrTe_3O_8$

S. Kabadou[1, 2], J. Horcheni[2,3]*, F. Mselmi[3], A. Kabadou[1], E. Dhahri[3] and L. Bessais[2]

[1]Laboratoire des Sciences des Matériaux et d'Environnement, Faculté des Sciences, Université de Sfax, 3000 Sfax, Tunisie.

[2]CMTR, ICMPE, UMR7182, CNRS - Université Paris Est Créteil, 2-8 rue Henri Dunant, F-94320, Thiais, France.

[3]Laboratoire de Physique Appliquée, Faculté des Sciences, Université de Sfax, 3000 Sfax, Tunisie.

Abstract

Polycrystalline $ZrTe_3O_8$:2%Er, 3%Mn was prepared by the solid-state reaction technique. The formation of single-phase material was determined by X-ray diffraction studies and found to be a cubic phase at room temperature. The structure can be described by two types of polyhedrons, namely disphonoids (TeO_4E with E = electronic lone pair of Te^{4+}) and octahedrons of ZrO_6. The bridges Te-O_1-Te and Te-O_2-Zr ensured the crystal structure cohesion. Both kinds of polyhedron oxygen were coordinated along the [010] mixed chain, linked to a pure chain of tellurium through O_1 in order to form a two-dimensional network and then a unit cell with a three-dimensional network. The Raman spectrum was dominated by a strong band at 841 cm^{-1}corresponding to Te-O_2-Zr bridges asymmetric stretching vibration. Consequently, the Te-O_2 and Zr (Mn)-O_2 bonds are chemically inequivalent and the Zr–O_2–Te bridges are chemically asymmetric. The magnetic results reveal the appearance of a weak ferromagnetic behavior at low temperature.The emission properties of the $ZrTe_3O_8$:2%Er, 3%Mn prepared at relatively high temperature examined at 490 nm excitation led to an appearance of an important emission in the visible and near-infrared domains due to homogeneously occupied Er^{3+} ions in the host lattice. Therefore, this kind of phosphors may be a meaningful reference for W-LEDs application.

Keywords: X-ray diffraction; Raman; Infrared spectroscopy; ferromagnetic; luminescence spectroscopy.

**Corresponding Author: Jihed HORCHENI*

E-mail: jihed.horcheni92@gmail.com

Introduction

Ceramics, known as non-metallic, non-amorphous materials and hence distinct from metal alloys and glasses, may be one of the oldest materials technologies, having been utilized for thousands of years.

Optical ceramics have been developed in industry for more than a half-century. These materials were created for specific applications requiring low cost, chemical resistance at high temperatures and pressures, or the greatest optical and dielectric quality are important. With a significant rise of activities in Light Emitting Diode (LED) related applications, LED-based solid-state technology is expected to gain more traction in human society. Phosphor-converted LEDs have recently brought improvements to next-generation solid-state smart invisible lighting technology, producing, for the first time, short-wave infrared (SWIR) light-emitting diodes (LEDs) [1]. In addition to (SWIR), red-emitting phosphors with a high quantum efficiency has great potential as they are utilized for warm-white LEDs and indoor plant cultivation [2, 3]. It is recognized that the phototropism reaction in green plants is very sensitive to the red light (610-700 nm), while the far-red light (700-740 nm) facilitates the photomorphogenesis of the plant. It would therefore be interesting to develop new phosphor materials with efficient red or far-red emission. Currently, red-emitting phosphors with a high quantum efficiency based on Eu^{2+} are commercially utilized for warm-white LEDs and plant growth field [3]. Contrary to the wide interest for the optical properties of Eu^{2+} as rare-earth activator for red emission less attention has been drawn to using Er^{3+} as dopant.

Dielectric ceramics for use in microwave resonators have received increased attention as a result of the rapid rise of mobile communication systems such as cellular phone, global positioning systems and personal communication system [4, 5]. Dielectric materials are often required to be co-fired with high conductivity electrons, as Ag and Cu to minimize the microwave absorption loss or to form a low-temperature co-fired ceramic (LTCC) technology [6, 7]. However, the sintering temperatures of common ceramics are in the range of 1200°C and 1500°C. Therefore, a considerable interest in developing novel materials with low sintering temperatures.

Recently, researchers demonstrated that the TeO_2-based ceramics technique had very low sintering temperatures ranging from 650 to 800°C and good microwave dielectric properties. [8]. This study aims to synthesize a stable and functional ceramic at hyper-frequencies (8-14GHz). For reducing sintering temperature, various additives were introduced into the formulation of the compositions, namely MnO_2 and Er_2O_3.

The objective of the present research work is to study the effect of doping zirconium by metal transition and rare earth on powder structure, spectroscopy characterization, optical and magnetic properties.

1. Experimental

The $ZrTe_3O_8$ was synthesized by the solid-state reaction method through the combination of two oxides, ZrO_2 and TeO_2. For 15 hours, the obtained mixture was calcined at 700°C, then the temperature started to decrease progressively until reaching room temperature with 40°/min rate. After that, the mixture was crushed for 30 min in agate mortar to obtain a fine powder of $ZrTe_3O_8$. Thus, the amount of MnO_2 and Er_2O_3 was added to the pure ceramic while respecting the doping percentages. Then, the resulting mixture was stirred in ethanol for one day after it was crushed. The polyvinyl (15% PVA) addition made the powder under the form of a paste that helps us to realize a palette that was pressed using a uniaxial pressure of 1 t/cm^2. Finally, the obtained pellet was sintered at 750°C for 10 hours.

For the X-ray diffraction, the studied sample was put in a sample carrier, and its analysis was realized to get information about its homogeneity and the phase purity. The data obtained by powder X-ray at room temperature were recorded by a SIEMENS D-5000 diffractometer equipped with a Cu X-ray source (with λ = 1.5406 Å) at 40 kW and 40 mA with constant (2θ) steps of 0.02. It was assumed that the mixed compound was isotopic with the $ZrTe_3O_8$ compound. Therefore, the Rietveld refinement [9, 10] was performed using FullProf software [11] to confirm our hypothesis. The Rietveld refinement was carried out with the pseudo-Voigt function [12] used for the simulation of the peak shapes. The diffractogram patterns with the addition of 2%Er, 3%Mn after sintering proved our compound's characteristic of single-phase oxide and isotopic with $ZrTe_3O_8$.

TGA measurements were carried out on 5-10 mg of the studied compound using a Perkine-Elmer TGA instrument. The analysis was conducted within a temperature range of 50-900 °C in a nitrogen atmosphere with a heating rate of $10°C.min^{-1}$.

The Raman spectra were realized in the 50-1200 cm^{-1} region using a system Horiba Jobin Yvon Spectrometer Micro Raman operating with source laser excitation and detector of 1024 pixels equipped with a liquid nitrogen-cooled CCD detector High sensitivity. Coherent radiation with a He-Ne laser at a wavelength of 633 nm and the output laser power at 50 mW was used to provide the excitation radiation. The spectral resolution in terms of slit width ranged from 3 to 1 cm^{-1}.

Magnetic measurements were performed using a physical property measurement system (PPMS) magnetometer from Quantum Design operating up to 9 T. The magnetic ordering temperature was determined from the temperature dependence of the magnetization measured in a magnetic field of 0.05 T in low temperature.

The absorption spectra obtained at room temperature were concluded about direct transmission measurement made with a spectrophotometer UV visible (HITACHY, U3300) in the range of 300-900 nm. The fluorescence spectrum at room temperature was deduced at 970 nm using a Perkin Elmer LS55 fluorescence spectrometer under excitation.

2. Structure determination

Figure 1 presents the Rietveld refinement plot. The resemblance between the calculated and the observed patterns proves the purity and the homogeneity of the prepared ceramic. Doped and undoped ceramics were found to crystallize with the same cubic space group of Ia-3 (N°206) and their unit cell parameters are close to each other ($ZrTe_3O_8$ a=11.3081 Å **[13]** and $ZrTe_3O_8$:2%Er, 3%Mn a=11.3160 Å).

Initially, we use Le Bail profile refinement to get the profile and instrumental parameters like zero error and asymmetry effect. The background was fitted with a linear interpolation between the 20 given points. The refinement with the unit cell parameters mixing with coefficient η, half-width parameters U, V, W, and the symmetry parameters converged to $\chi^2 = 2.96$. Next, the proposed structure was refined while fixing the profile and instrumental parameters. Finally, refinement takes into consideration the overall isotropic displacement factor converged to R_p= 18%, R_{wp}=21.5%, R_{exp}=12.47%, thus R_F= 3.68% and R_{Bragg}=5.40% are less than 10%, implying the obtained results are reliable. The occupancy probability of the Zr, Er, and Mn was refined in such a way that the 8(a) was entirely occupied. While crystal structure data and experimental conditions are collected in **Table 1**, position and isotropic thermal parameters are presented in **Table 2.**

A perspective view of the unit-cell content is shown in **Figure 2**. In fact, the structure is formed by the octahedron of zirconium and the tetrahedron of tellurium connecting to each other through two types of oxygen. In addition to Te-O_1-Te-O_2-Zr-O_2, with a boat conformation (**Figure 3(a)**), four isomers of Te_2ZrO_3 connected through Zr atoms (**Figure 3(b)**) have been characterized, forming a tunnel along the c axis. The tricyclic Te_3ZrO_4 (**Figure 3(c)**) is derived from Te_2ZrO_3 by the formal insertion of a Te-O_2 bridge.

2.1. Environment of Te atoms

The environment of tellurium atoms consists of polyhedron in view of distorted trigonal bipyramids TeO_4E. Its equatorial planes contain the two short bonds (formed by Te and O_2 types), and the lone pair (E) occupies the third equatorial position, whereas the axes are formed by their two long bonds (under the form Te-O_1). The Te-O bond lengths are in the range of 1.86165(6)Å-2.17794(10) Å and the O-Te-O angle vary from 79.4(10) to 160.8 (13) °. The high anisotropy of the Te atom can be justified by the distribution of the chemical bonds. This asymmetry emanates from the existence of the stereo-active lone pair $5s^2$. The Te-O chemical bonds are presented on one side of the Te atom. Besides, the lone pair E monopolizes the other side that forms a 'dead zone'. The two non-bondings Te-O (2.933 Å) form 'empty' cavities. The four-coordinated TeO_4 was interconnected by a common corner through O_1 to form a pure zigzag chain parallel to [010] direction (**Figure 4**).

2.2. Environment of Zr/Mn/Er atoms

The Zr was six-fold coordinated with O_2-type oxygen atoms composing a slightly distorted octahedron with Zr/Mn/Er-O distance of about 2.07405(7) Å and O- Zr/Mn/Er-O angle varying from 88.5° to 180°.The ZrO_6 sharing the O_2 corners with the disphonoids of the tellurium to form an infinity of mixed chains parallel to the b axis. The pure chain formed by TeO_4 is linked to the mixed chain through the oxygen atoms O_2 to form a three-dimensional structure (**Figure 5**).

2.3. Doping effect on crystallographic parameters

The substitution of the zirconium by two cations with the same and lower valence, such as Er^{3+} and Mn^{4+} in the base compound $ZrTe_3O_8$ made a bond distance change. The lattice parameters for three samples: $ZrTe_3O_8$ and $ZrTe_3O_8$: 2%Er 3% Mn, are collected in **Table 3.** Although the cubic system and the space group Ia-3 remained, the volume of the unit cell simultaneously increased with the increase of the doping percentage. The Zr-O_2 bond distance is the biggest bond, which can be explained by the susceptibility of manganese to remove the oxygen atom **[14]**, and therefore the increase of Te-O_2. The Er^{3+} plays the reverse role of the Mn^{4+} even in a small amount, which was unexpected in our synthesized powder.

3. Thermal analyses

The TGA result of $ZrTe_3O_8$ with 2% Er_2O_3 and 3% MnO_2 is presented in **Figure 6**, revealing no weight loss associated with the melting reaction. The TG curve of our ceramic shows that our simple phase is stable up to 750°C. The decrease in weight with temperature is primarily due to the evaporation of the volatile species, which is observed at temperatures above 800°C.

4. Spectroscopy study

The Raman study was restricted to the frequenciesranging from 50 to 1200 cm^{-1}. The superposition of the two Raman spectra of the pure and the doped ceramic at room temperature is given in **Figure7,** where it shows the presence of an intense peak at 105 cm^{-1} accompanied by a shoulder (142 cm^{-1}) corresponding to translation and rotation movements of isolated TeO_2 entities, respectively **[15, 16]**.The symmetric stretching vibration of Te-O-Zr bridges gives birth to a band located near 454 cm^{-1}, while a very intense band appears at 853 cm^{-1} corresponding to the asymmetric stretching **[14]**.

In the pure ceramic $ZrTe_3O_8$, the long bond of Te-O_2 and Zr-O_2 were 1.858(2) Å and 2.073(2) Å, respectively **[13]**. There is a noticeable difference between these two values that were not chemically equivalent, which can be shown by the Raman spectrum of $ZrTe_3O_8$ through the existence of an important band around 855 cm^{-1} attributed to the asymmetric stretching vibration of Te-O_2-Zr bridges, while the doping compound (2%Er and 3%Mn) increased the difference between the two lengths of Te-O_2 and Zr-O_2, thus obtaining more chemical equivalent bands. Te-O_2 length was 1.86165(6)Å and that of Zr-O_2 was 2.07405(7)Å, which resulted in less asymmetric Te-O_2-Zr bridges. Therefore, the Raman spectrum proved the appearance of a weak band around 450 cm^{-1} and intense band around 840 cm^{-1}. It illustrates that the Te-O_2-Zr bridges were more asymmetrical in the pure ceramic than Te-O_2-Zr observed in $ZrTe_3O_8$:2%Er, 3%Mn. The synthesized ceramic demonstrates a decrease in the intensity of the band 590 cm^{-1} shown in the pure ceramic, thus obtaining a less distorted trigonal bipyramid TeO_4. The Raman measurement shows that doping $ZrTe_3O_8$ with Er^{3+} and Mn^{4+} in certain attractive changes, such as the spectrum of the pure ceramics having a sharp and intense peak compared to the doped one. Then, the synthesized ceramic spectrum shifts to the low-frequency region. For more illustration, we chose to realize the Raman spectrum deconvolution for the doped and the pure ceramics between 50 and 1200 cm^{-1} **(Figure 8)**. In order to facilitate discussion, we divided the Raman spectra into three regions:

- **The first region between 50 and 240 cm^{-1} frequency range**

The five modes observed at 60, 80, 108, 143 and 190 cm^{-1} in $ZrTe_3O_8$ are conserved in the doped compound with overlap between the peaks. The intense peak (105 cm^{-1}) accompanied by a shoulder (140 cm^{-1}) corresponding to the translation and rotation movements of isolated TeO_2 entities, respectively.

- **The second region between 240 to 600 cm^{-1}**

Enlargement of the band around 284 cm^{-1}.

The enlargement and decrease of the intensity band observed in 450 cm^{-1} can be attributed to the symmetric stretching vibration of Te-O(2)-Zr/Er/Mn.

- **The third region between 620 to 1200 cm^{-1}**

There exists an overlap and increase in intensity between the four bands observed at 670, 750, 780 and 853 cm^{-1}. At 841 cm^{-1}, we observed the existence of an important band corresponding to the asymmetric stretching vibration of the Te-O(2)-Zr/Er/Mn bridges.

According to the results provided by the Raman measurements at room temperature, it can be confirmed that the substitution of Zr^{4+} with Mn^{4+} and Er^{3+} in the matrix of $ZrTe_3O_8$ created more bridging in the framework of the structure without changing the whole symmetry, hence confirming the results of XRD measurements.

5. Fluorescence spectra

The absorption spectra **(Figure 9)** of $ZrTe_3O_8$: 2% Er, 3% Mn at room temperature (T=300K) shows several sharp Er^{3+} lines. A sharp intense peak at 310 nm (32679 cm^{-1}) assigned to the transitions from the ground state $^4I_{15/2}$ to the sublevel of $^4G_{5/2}$. In addition to this sharp intense peak, typical broad excitations bands of Er^{3+} due to the transition from $^4I_{15/2}$ to the crystal field sublevels of $^2H_{9/2}$ (410 nm) and $^4S_{3/2}$ (550 nm) are observed. A very sharp and strong absorption lines around (710 nm) and (820 nm) are also observed due to the replica phonon of the transitions $^4I_{15/2} \rightarrow {}^4F_{9/2}$ and $^4I_{15/2} \rightarrow {}^4I_{9/2}$.

The PL spectra of $ZrTe_3O_8$:2% Er,3% Mn obtained at room temperature under λ_{ex} =490 nm =20408 cm^{-1} (**Figure 10**) reveals three major spectrum components: a sharp and strong intense band E_{PL1} centered around 735 nm (13605 cm^{-1}), a very weak broad emission bands E_{PL2} between 600 nm and 670 nm and a weak broad emission band E_{PL3} from 800 nm to 840 nm. Based on the excitation and PL analyses these emission bands are due respectively to the transitions $^4F_{7/2} \rightarrow {}^4I_{13/2}$, $^4F_{9/2} \rightarrow {}^4I_{15/2}$ and $^4S_{3/2} \rightarrow {}^4I_{13/2}$. These transitions have the same energy location in the experimental excitation and emission spectrums of Er^{3+} in Gd_2O_3 nanocrystals [17]. The theoretical calculation presented by *Chen et al* [17] reproduces well the transitions involved in the absorption and emission spectrums in accordance with wavelength excitation.

this tranches in favor for the validity of the attribution of absorption and emission bands. These assignments are reasonable since rare earth ions are insensitive to their surroundings environment and act almost like free ions.

Figure 11 shows a CIE1931 chromaticity diagram for the Er-Mn-ZTO ceramic. The calculated coordinates concentrate at 0.73 and 0.25, and overlap under the 490 nm light excitation. The color coordinates locate within the red-orange region, which agrees well with the strong photoluminescence emission of the $^4F_{7/2} \rightarrow {}^4I_{13/2}$ transition and luminescent images.

The $ZrTe_3O_8$:2% Er, 3% Mn phosphor exhibits red emission in the range 610 nm- 740 nm. A strong far-red emission at 735 nm which match well with the absorption band of phytochrome **[18]**. In fact, the phototropism reaction is very sensitive to the red light (610-700 nm) while the far-red light (700-740 nm) facilities the photomorphogenesis of the plant **[2, 18]**. The $ZrTe_3O_8$:2% Er, 3% Mn phosphor have great potential as far–red emission phosphors in plant growth LEDs.

6. Magnetic properties

As one of our objectives is to associate the physical properties, we undertook a study of magnetic properties consisting of $ZrTe_3O_8$: 2%Er, 3%Mn. The doping by the rare earth and the transition metal is the responsible for creating magnetic properties in the tellurium family. The material magnetization depends on two variables, namely applied magnetic field and temperature. The magnetic measurement of the doped ceramic was performed in the [5-300 K] temperature range, using a magnetometer Physical Properties Measurement System (PPMS).

First of all, the $ZrTe_3O_8$: 2%Er, 3%Mn was put at room temperature in the absence of a magnetic field. Then, the temperature decreases progressively by applying a moderate measuring field (H=0.05T), and the values of the magnetization were registered. The magnetization curve showed in **Figure 12** reveals that the doped ceramic exhibits a magnetic transition from a ferromagnetic to a paramagnetic state. The Curie temperature that was estimated using the numerical derivative dM/dT is exhibited in the inset of **Figure 12** for our compound from which the Curie temperature T_C is less than 5K.

In fact, the ferromagnetic material loses its spontaneous magnetization, exceeding the Curie temperature, and therefore the materials become disordered and thus called paramagnetic. Although the material regains their ferromagnetic properties by getting closer to the Curie temperature, it is a reversible phase transition.

The inverse of magnetic susceptibility is plotted in **Figure 12**, it was analyzed using a Curie-Weiss law **[19]** to understand the effect of partial doping in the paramagnetic region:

$$\chi = \frac{C}{(T-\theta p)} \qquad (1)$$

θp: Weiss temperature and the Curie constant C are defined as follows:

$$C = \frac{Ng^2\mu_B^2 J(J+1)}{3K_B} = \frac{N\mu_B^2}{3K_B}\mu_{eff}^2 \qquad (2)$$

where N_A=6.02310^{23} mol^{-1} refers to the number of Avogadro, μ_B= 9.2741021emu refers to the Bohr magneton, and k_B= 1.3801610^{-16} erg k^{-1} refers to the Boltzmann constant.

Based on the Curie constant value, we calculated the experimental effective moment μ_{eff}^{exp} (in a unit of Bohr magneton μ_B) from the following relation:

$$\mu_{eff}^{exp} = (\sqrt{8C})\mu_B \qquad (3)$$

The intersection with the real axis gives Weiss temperature value θ_p, and the Curie constant was determined by the slope. From these data, the effective moment was calculated in the paramagnetic phase.

According to the electronic configuration of the only magnetic element, the effective theoretical **[19]** moment can be expressed as:

$$\mu_{eff}^{The} = g_j\sqrt{J(J+1)}\mu_B \qquad (4)$$

Where μ_{eff} is the effective paramagnetic moment, g_J is the gyromagnetic factor and J=L+S is the total orbital moment.

The theoretical value of the effective moment of $Mn^{4+}$is calculated by:

$$\mu_{eff}^{The}(\mathrm{Mn}^{4+}(3d^3)) = g\sqrt{s(s+1)} = 3.87\mu_B$$

with g=2, and S=3/2 for Mn^{4+}.

However, the theoretical value of the effective moment from the rare earth Er^{3+} is given by:

$$\mu_{eff}^{The}(\mathrm{Er}^{3+}(3d^{11})) = g\sqrt{J(J+1)} = 9.58\mu_B$$

with L=6, S=3/2, J=15/2

The theoretical effective moment of $ZrTe_3O_2$: 2%Er, 3%Mn taking into consideration the rigid coupling between the ions Er^{3+} and Mn^{4+} can be given by the following relation:

$$\mu_{eff}^{The}(ZrTe_3O_8 : 2\%Er,\ 3\%Mn) = \sqrt{0.02\mu_{eff}^{The}(Er^{3+})^2 + 0.03\mu_{eff}^{The}(Mn^{4+})^2}$$

Curie Constant (C), Weiss temperature (θ_p), the experimental and the theoretical value of paramagnetic moment are shown in **Table 4.**

The experimental values of the effective moment are high as the theoretical values. This result can be explained by the existence of a short-range ferromagnetic interaction in the paramagnetic phase. As the θ_p has a positive sign, the ferromagnetic interaction is highly expected in this material [19, 20].

Figure 13 displays hysteresis loops for the $ZrTe_3O_2$: 2%Er, 3%Mn measured at temperature of 10 K measured in a magnetic field range up to 9T. In order to quantify the magnetic parameters like saturation magnetization M_s, intrinsic coercivity H_c, and remanent magnetization M_r, and better understand the contribution of Ferromagnetic and Antiferromagnetic domains, a theoretical model was replicated, described by the following equation [21]:

$$M(H) = \left[2\frac{M_{FM}^{S}}{\pi} artan\left(\left(\frac{H \mp H_c}{H_c}\right) tan\left(\frac{\pi * r}{2}\right)\right)\right] + \chi H \qquad (5)$$

Where M_{FM}^{S} , H_c, r and χ are the saturation magnetization for the ferromagnetic contribution, the coercive magnetic field, the rapport M^R/M^S and magnetic susceptibility, respectively. The first term corresponds to the ferromagnetic contribution, while the second term represents the antiferromagnetic one. The adjusted parameters are summarized in Table 4. Consequently, this sample is soft magnetic materials (H_c=141 Oe). Therefore, the studied compound are promising candidates to be used in the electrical machine and transformer inductors and inductive components, low- and high-frequency transformers, motors and generators, high-frequency inductors and absorbers; magnetic and magneto-mechanical sensors.

7. Impedance analysis

The conduction mechanism and the electrical process are interpreted by the technique of complex impedance spectroscopy. This procedure is useful to study separation of the electrical response refer to the grain, grain boundary, and electrode polarization in a ceramic sample with a different relaxation time [22].

To explain the contribution of the grain and grain boundaries, we plotted the Nyquist diagram of our doped sample (Z" versus Z') for some representative temperature Figure 14. The complex impedance of doped compound can be represented as:

$$Z^*(\omega) = Z'(\omega) - j\,Z''(\omega)$$

Where Z' is the real part and Z" is the imaginary part of Z^*.

The spectra of the complex impedance at different temperatures show that $ZrTe_3O_8$:2%Er, 3%Mn follows the Cole-Cole law. In this instance, the center of a semi-circle presented in Figure 14 at definite temperature is removed under the axis of Z' $(\alpha = (1-\beta)\frac{\pi}{2})$

[23]. The insert of Figure 14 indicates the variation of the β angle at different temperatures. We can deduce that the value of the β decreases when the temperature increases that can demonstrate a large relaxation time width distribution compared with Debye relaxation type [24].

The variation of the imaginary part of impedance (Z_{Img}) with frequency at different temperatures is presented in Figure 15. The ZrTe3O8:2%Er,3%Mn, explains the presence of one relaxation process and is more evident. With increasing temperature, we see the peak shift to the higher frequency side and the maximum value of Z_{Img} drop. It is important to note the presence of a symmetric peak which is related to the grain relaxation.

As shown in Figure 15, the maxima in Z" shift to the higher frequency, with increasing temperature, and correspond with the theoretical model [25] which describes the difference of energy between the valence band and the trap level calculated by using the equation:

$$f_{max} = f_0 \exp\left(\frac{-E_a}{k_B T}\right)$$

Where f_{max} presents the maximum frequency of Z'', T is the temperature, and k_B the Boltzmann constant. The insert of Figure 15 shows the variation of $Ln(F_{max})$ as a function of 1000/T. From this plot, we can deduce that E_a=0.34 eV.

Figure 16 shows the deconvolution of Z" at T=700K using one peak corresponding to the grain response.

Conclusion

$ZrTe_3O_8$ doped 2%Er,3%Mn was successfully synthesized by the solid state reaction method. The structure refinement has proven that the new ceramic crystallizes in the cubic system with I a-3 space group. $Zr/Er/MnO_6$ was connected by TeO_4E groups with Zr/Er/Mn-O-Te and bonding contacts. The RAMAN spectrum allowed to mark the vibrational band relative to TeO_4, the symmetric and the asymmetric stretching vibration of Te-O-Zr bridges. The magnetic analysis revealed that our sample exhibited a paramagnetic - ferromagnetic transition with a Curie temperature below 5K. Finally, the emission properties of the synthesized compound examined at 490 nm excitation led to an appearance of an important emission in the visible and near-infrared domains.

The CIE value fully achieves the standard red color coordinates (0.73 and 0.25). Therefore, this kind of phosphors may be applied to W-LEDs and plant growth field.

Declaration of interests

The authors declare that they have no known competing financial interests or personal relationships that could have appeared to influence the work reported in this paper.

Acknowledgment

The authors acknowledge the support of the Tunisian Ministry of Higher Education and Scientific Research and the French Ministry of Higher Education andScientific Research within the framework of the Franco-Tunisian collaboration.

References

[1] Lifang Yuan, Yahong Jin, Haoyi Wu, Kaiyuan Deng, Bingyan Qu, Li Chen, Yihua Hu, and Ru-Shi Liu *ACS Applied Materials & Interfaces* 2022 *14* (3), 4265-4275

[2] Yibing Wu, Ying Lv, Kaibin Ruan and Zhi Xie , Dalton Trans. 2018,471557

[3] M. Zhu, Y. Pan, L. Xi, H. Lian and J. Lin, J. Mater. Chem. C, 2017, 5, 10241.

[4] Y. Imanaka: Multilayered Low Temperature Cofired Ceramic Technology (LTCC) (Springer, New York, 2005) 1st ed., pp. 1–15.

[5] H. Jantunen, R. Rautiaho, A. Uusimaki, S. Leppavouri, Ceram. Soc. 20 (2000) 2331.

[6] J.W. Sheen, IEEE Microw. Wave Lett. 10 (2000) 92-93

[7] Xiaoli Zhu, Zhonghua Wang, XinmingSu, Paula M. Vilarinho, ACS Appl. Mater.Interfaces 6 (2014) 11326-11332.

[8] O. Yamaguchi, T. Ohtagaki, K. Shimizu, Z. Anorg. Allg. Chem. 564 (1988) 115.

[9] H.M. Rietveld, J. Appl. Cryst. 2 (1969) 65-71.

[10] A. Taoufyq, D.V. Chokouadeu, B. Bakiz, H. AitAhsaine, L. Patout, A. Benlhachemi, M. Ezahri, F. Guinneton, A. Lyoussi, G. Nolibe, J-R. Gavarri, J. Mater. Environ. Sci. 5 (S2) (2014) 2550-2554.

[11] J. Rodríguez-Carvajal, "FullProf: A program for rietveld refinement and pattern matching analysis," Satellite Meeting on Powder Diffraction of the XV Congress of the IUCr, Toulouse, France, (1990) 127.

[12] R.A. Young, D.B. Wiles, J. Appl. Crys. 15 (1982) 430-438.

[13] G. Meunier, J. Galy, Acta.Cryst. B27 (1971) 602.

[14] M. Koubaa, R. Karray, N. Dhifallah, A. Kabadou, L. Bsais, J. AlloysCompd. 709 (2017) 808-818.

[15] R.D. Shannon, Acta Crystallogr. A 32 (1976) 751-767.

[16] M. Dutreilh, P. Thomas, J.C. Champarnaud- Mesjard, B. Frit, Solid State Sci. 3 (2001) 423.

[17] Xueyuan Chen, En Ma, and Guokui LiuJ. Phys. Chem. C 111 (2007) 10404-10411

[18] Jianxu Hu, Tinghong Huang, Yuanpeng Zhang, Bin Lu, Huanqing Ye, Baojiu Chen, Haiping Xia and Changyan Ji, Dalton Trans 48(7) (2019) 2455-2466

[19] S. Gharbi, Y. Marouani, F. Issaoui, E.Dhahri, E.K. Hlil,R. Barille, B.F.O.Costa, J. Mater. Sci: Mater. Electron, 31 (2020) 11983–11996

[20] Kittel C. Introduction to Solid State Physics. 6th edn. NewYork: Wiley, 1986, 404.

[21] Y. Marouani, A. Mabrouki, R. Dhahri, E. Dhahri, B.F.O. Costa, Inorg. Chem. Commun. 136 (2022) 109163.

[22] J.R. Macdonald, Impedance Spectroscopy: Emphasizing Solid State Materials and Systems, Wiley, New York. (1987) Chapters 2 and 4.

[23] J.R.M. E. Barsoukov, Impedance Spectroscopy: Theory, Experiment,and Applications, John Wiley & Sons, New York, John Wiley Sons, New York. (2005).

[24] L. Essaleh, G. Marín, S.M. Wasim, S. Lahlali, H. Chehouani, Analysis of complex impedance of p-CuIn3Se5by impedance spectroscopy, J. Alloys Compd. 688 (2016) 210–215.

[25] H.T rabelsi, M. Bejar, E. Dhahri, M. Sajieddine, K. Khirouni, P.R. Prezas, B.M.G. Melo, M.A. Valente, M.P.F. Graça, J. of Alloys and Comp., 723(5) (2017) 894.

Captions Figure

Fig 1: Rietveld refinement of XRD pattern for $ZrTe_3O_8$:2%Er, 3%Mn. The circles are the observed profile; the solid line is the calculated one. Tick marks below the profile indicate the position of allowed Bragg reflections.

Fig 2: The chains of the three-dimensional network.

Fig 3: (a,b) Structural frameworks of isomer Te_2ZrO_3 and Te_3ZrO_4 in a boat conformation (c) Framework of tellurium and titanium polyhedra in the $ZrTe_3O_8$: 2%Er, 3%Mn structure.

Fig 4: Environment of Te atoms.

Fig 5: Interconnecting of zirconium neighboring.

Fig 6: TGA curve of $ZrTe_3O_8$:2%Er, 3%Mn

Fig 7: Evolution of the Raman spectra of $ZrTe_3O_8$ and $ZrTe_3O_8$:2%Er, 3%Mn ceramics at room temperature.

Fig 8: Raman deconvolution of the $ZrTe_3O_8$ and the doped ceramic $ZrTe_3O_8$: 2%Er, 3%Mn at room temperature in different regions.

Fig 9: Absorption spectrum of $ZrTe_3O_8$:2%Er,3%Mn.

Fig 10: Evolution of photoluminescence (PL) spectra of $ZrTe_3O_8$: 2%Er,3%Mn ceramic.

Fig 11: CIE Chromaticity for $ZrTe_3O_8$: 2%Er,3%Mn

Fig 12 Variation of the magnetization and the inverse of the susceptibility as a function of temperature for $ZrTe_3O_8$:2%Er, 3%Mncompound under an applied magnetic field of 0.05T. The inset displays dM/dT versus T

Fig 13: Hysteresis loops fitted by Equation (5)for $ZrTe_3O_8$:2%Er,3%Mn samples at 10K.

Fig 14: Complex impedance curves of ZrTe3O8:2%Er, 3%Mn compound at various temperatures.

Fig. 15: Variation of Z" as a function of the frequency for some representative temperatures. The insert represents the variation of Ln(fmax), deduced from the maximum of Z'', as a function of 1000/T

Fig.16: The deconvolution of Z'' with frequency at 700K.

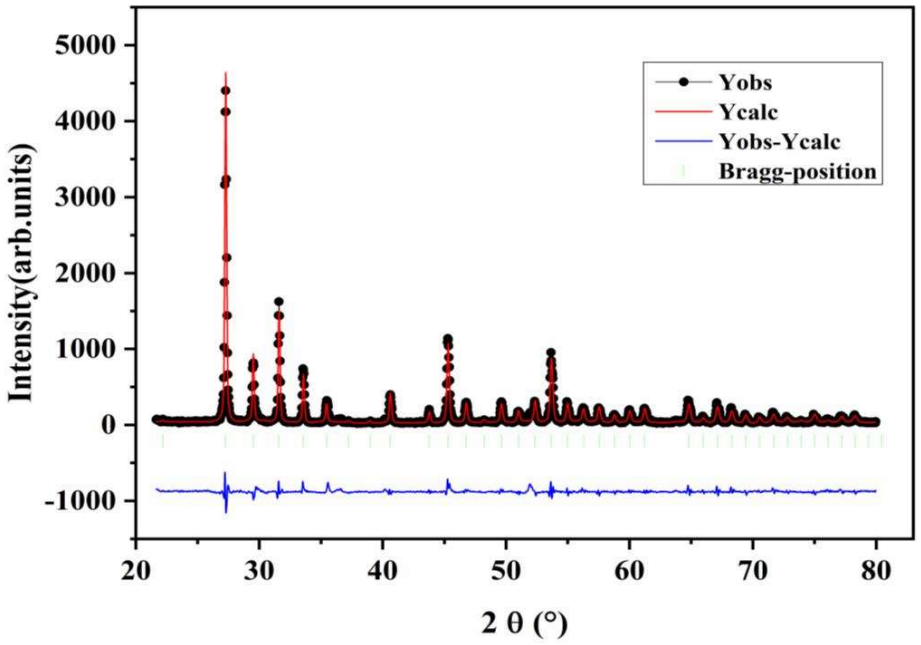
Yobs
Ycalc
Yobs-Ycalc
Bragg-position
Intensity(arb.units)
5000
4000
3000
2000
1000
0
-1000
20
30
40
50
60
70
80
2 θ (°)

Fig 1

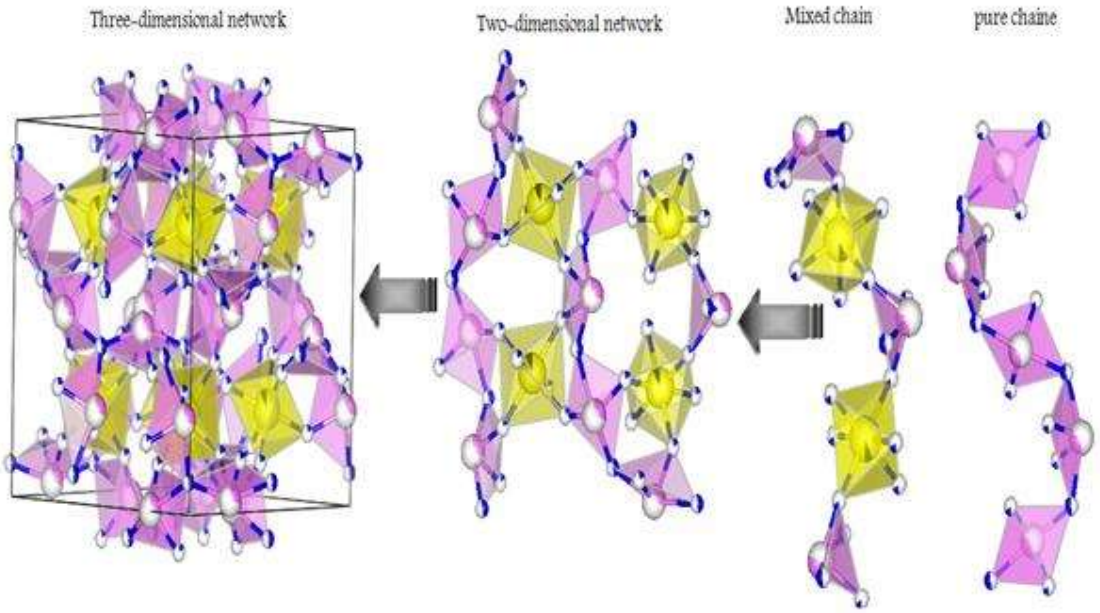
Three-dimensional network
Two-dimensional network
Mixed chain
pure chaine

Fig 2

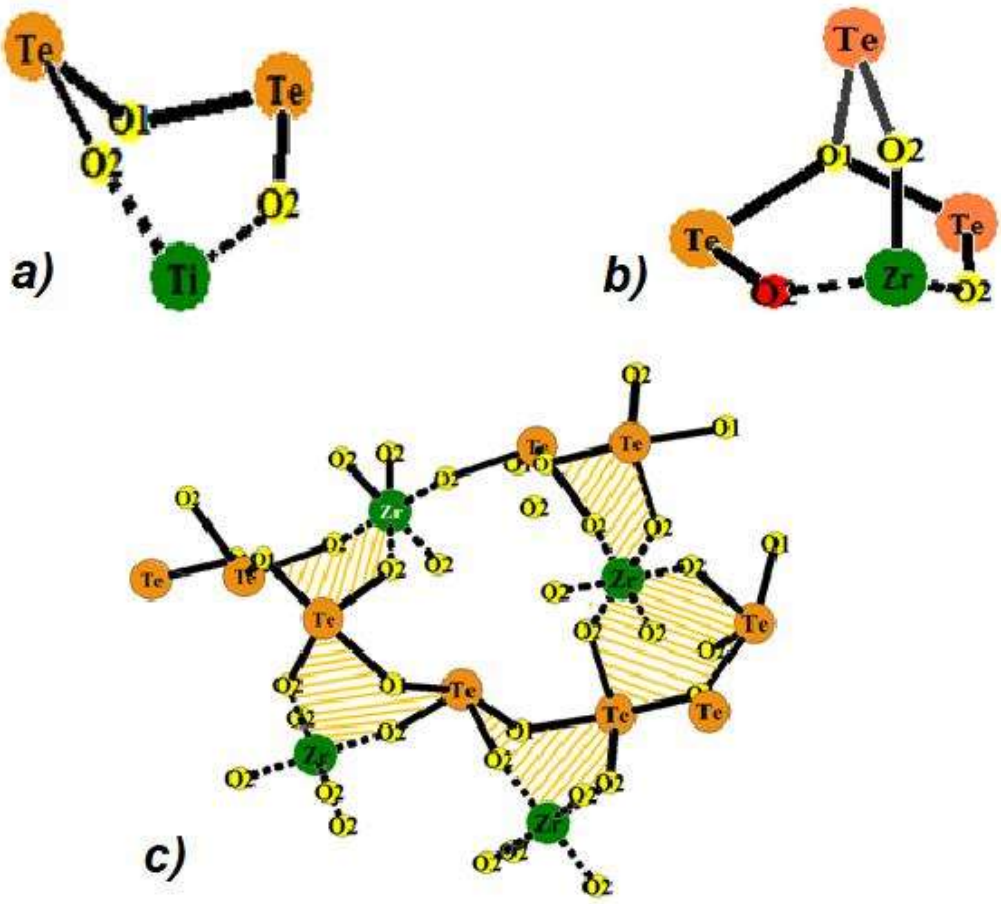

Fig 3 a) b) c)

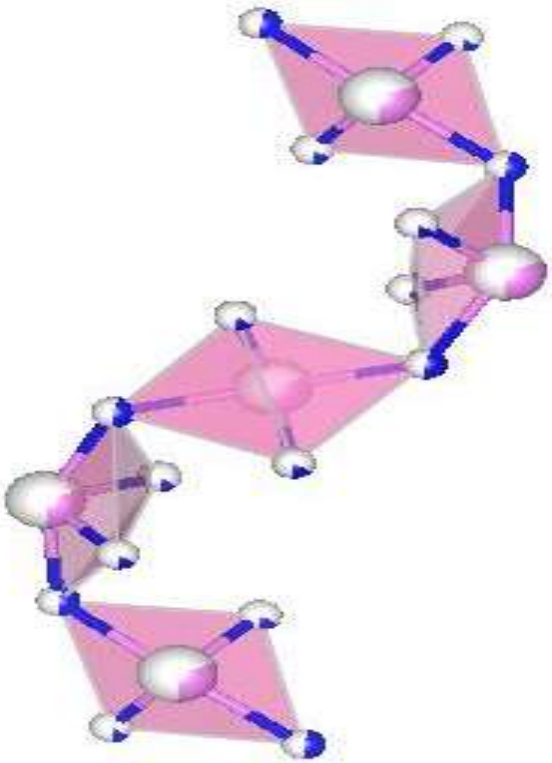

Fig 4

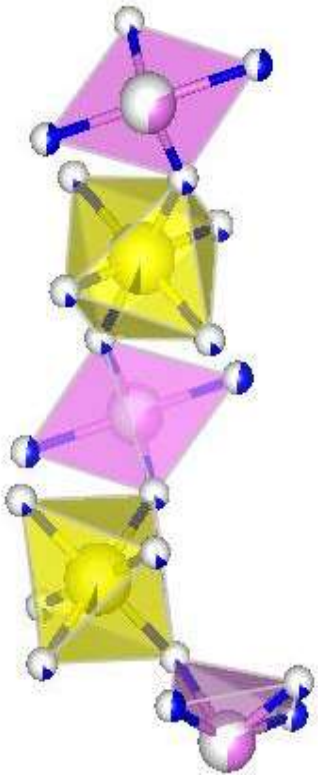

Fig.5

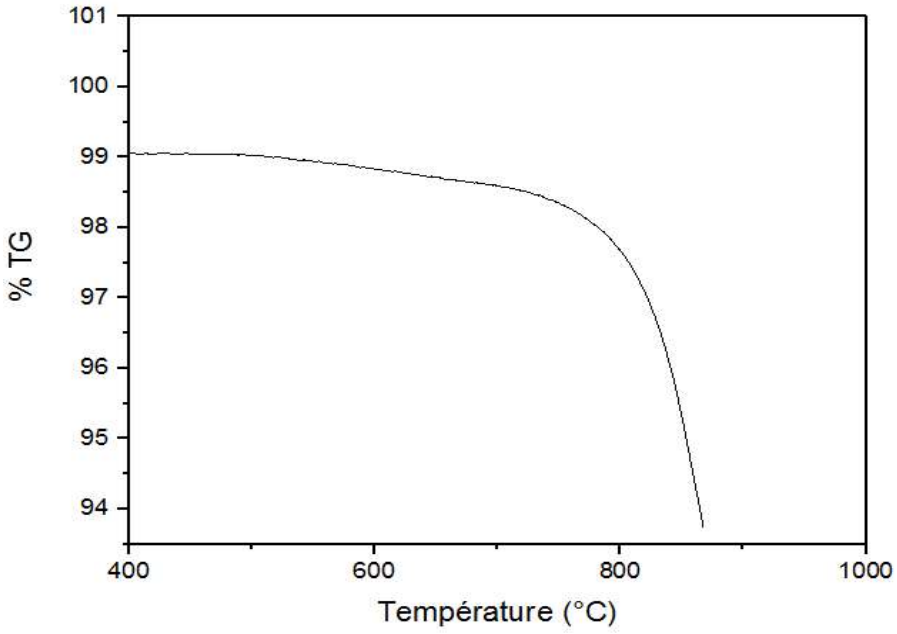

Fig.6

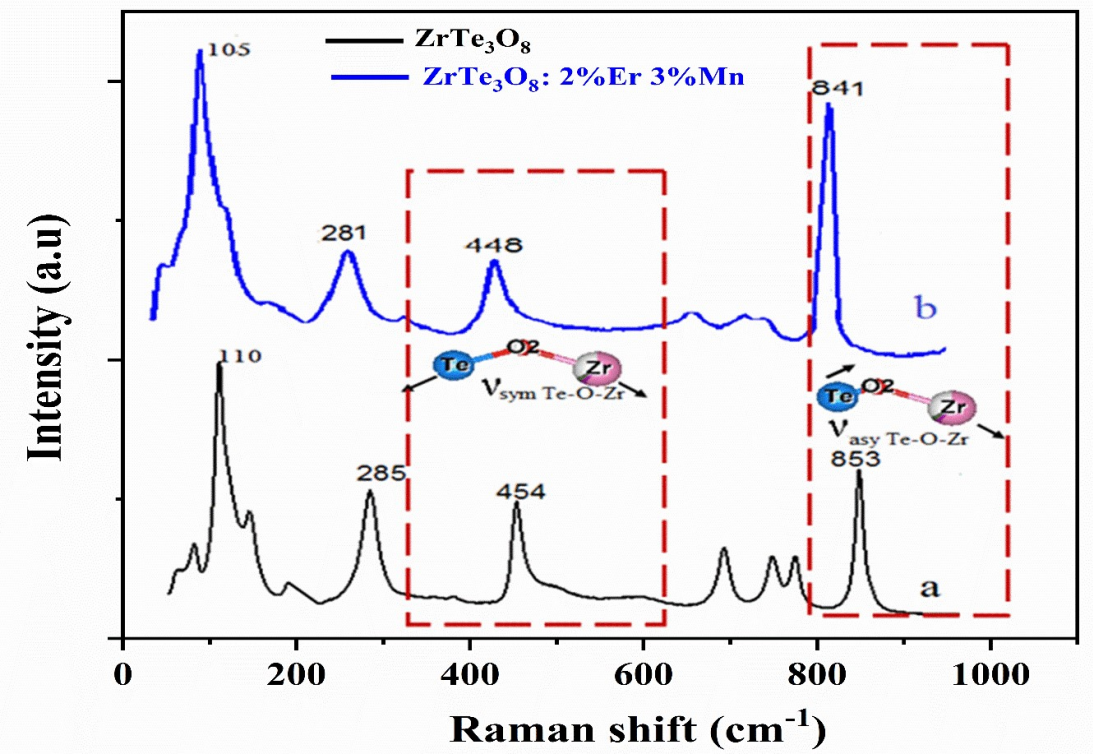
ZrTe3O8
ZrTe3O8: 2%Er 3%Mn
105
281
448
841
b
110
285
454
853
a
Te
O2
Zr
νsym Te-O-Zr
νasy Te-O-Zr
Intensity (a.u)
0
200
400
600
800
1000
Raman shift (cm-1)

Fig.7

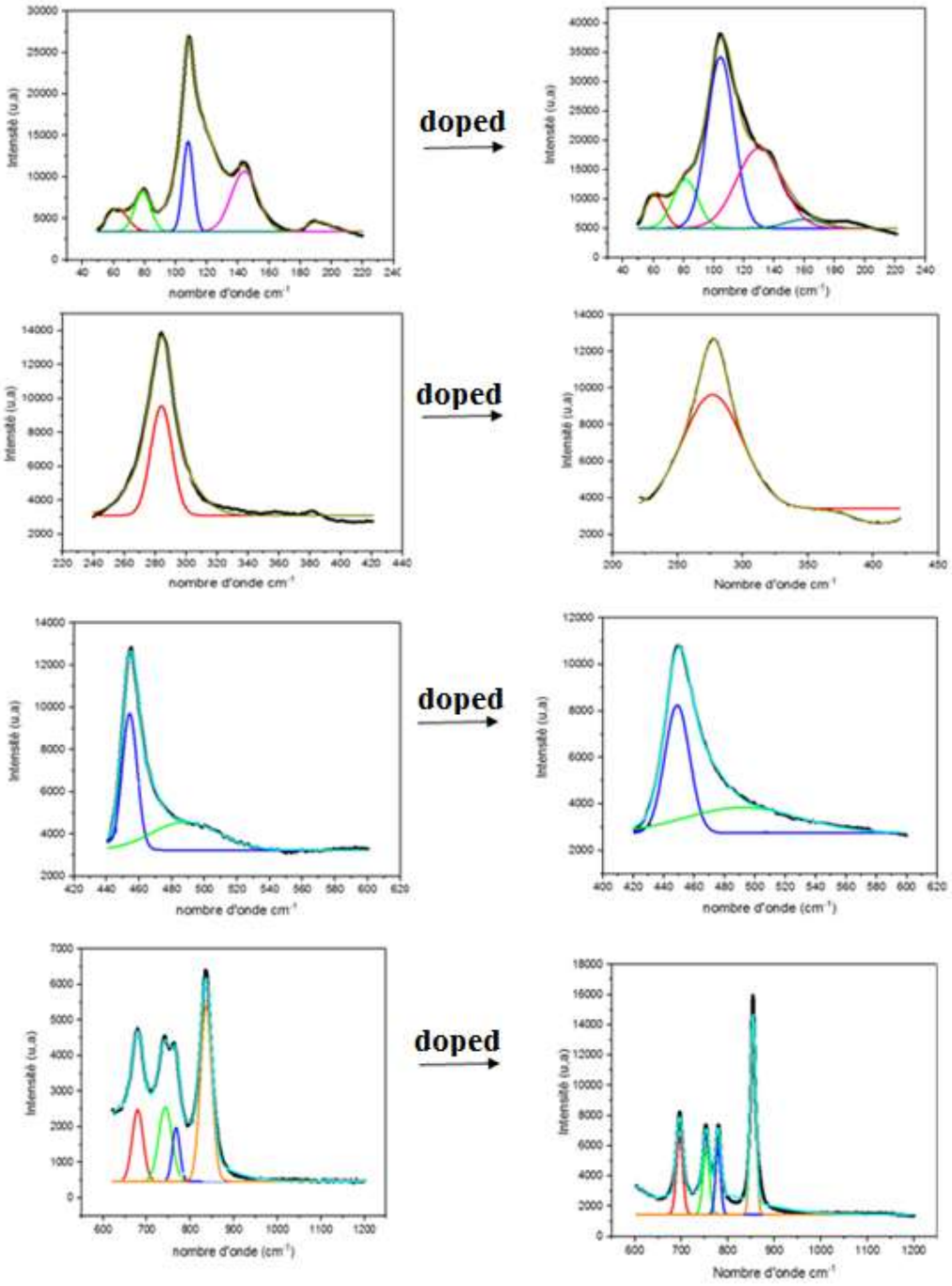
doped
doped
doped
doped
Intensité (u.a)
nombre d'onde cm-1
nombre d'onde (cm-1)
Nombre d'onde cm-1

Fig.8

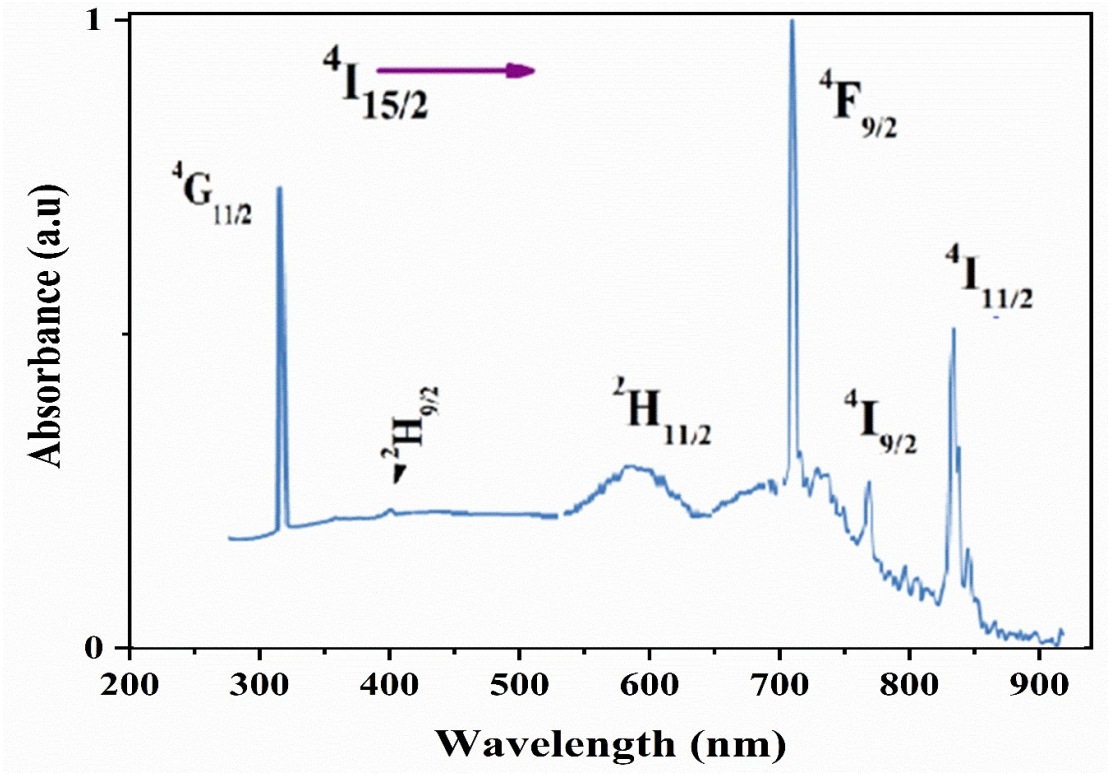
1
0
Absorbance (a.u)
200
300
400
500
600
700
800
900
Wavelength (nm)
$^4I_{15/2}$
$^4G_{11/2}$
$^2H_{9/2}$
$^2H_{11/2}$
$^4F_{9/2}$
$^4I_{9/2}$
$^4I_{11/2}$

Fig 9

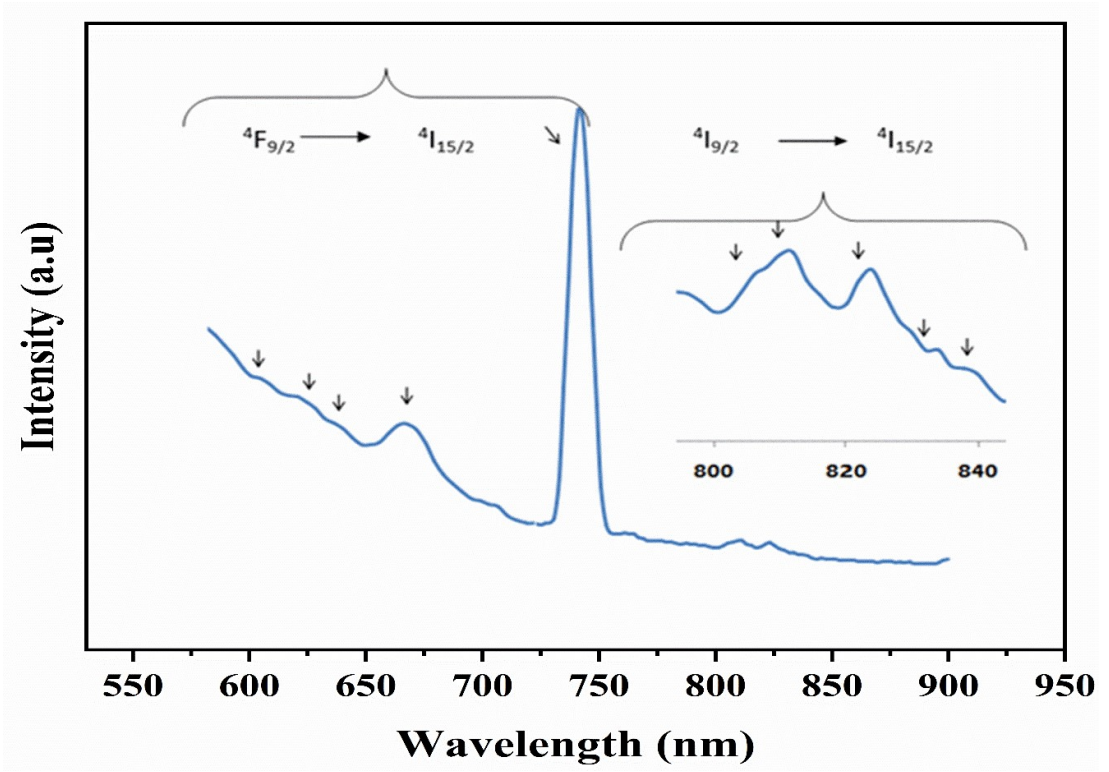
Intensity (a.u)
550
600
650
700
750
800
850
900
950
Wavelength (nm)
$^4F_{9/2}$ → $^4I_{15/2}$
$^4I_{9/2}$ → $^4I_{15/2}$
800
820
840

Fig.10

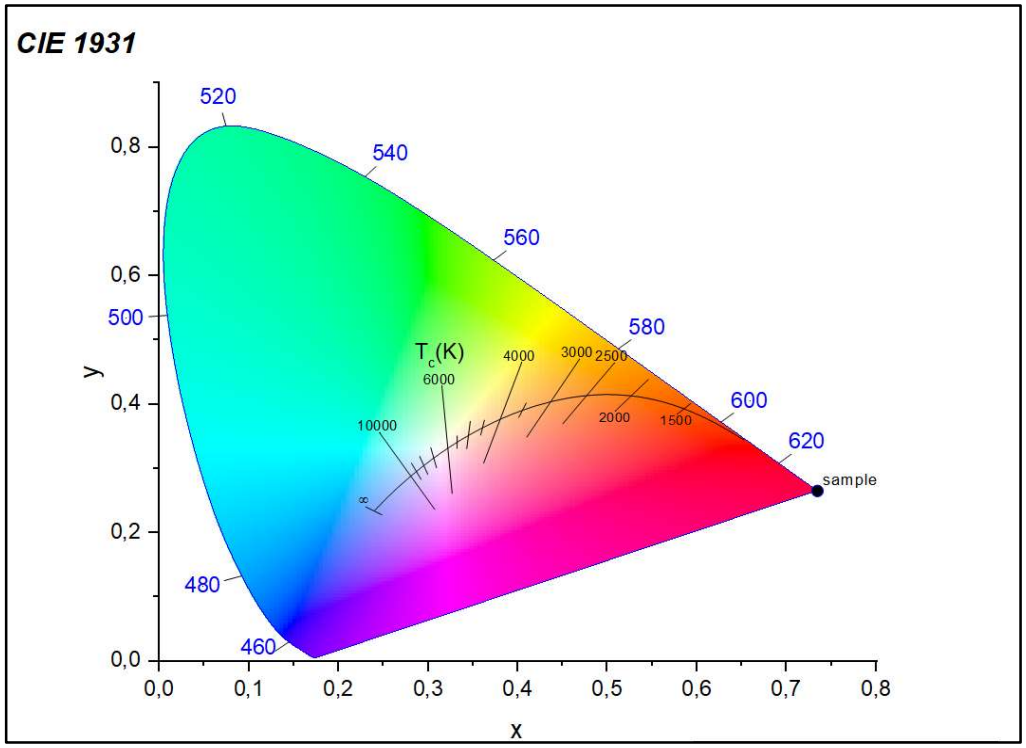
CIE 1931
520
540
560
580
600
620
500
480
460
sample
T_c(K)
6000
4000
3000
2500
2000
1500
10000
∞
y
x
0,0
0,2
0,4
0,6
0,8
0,1
0,3
0,5
0,7

Fig.11

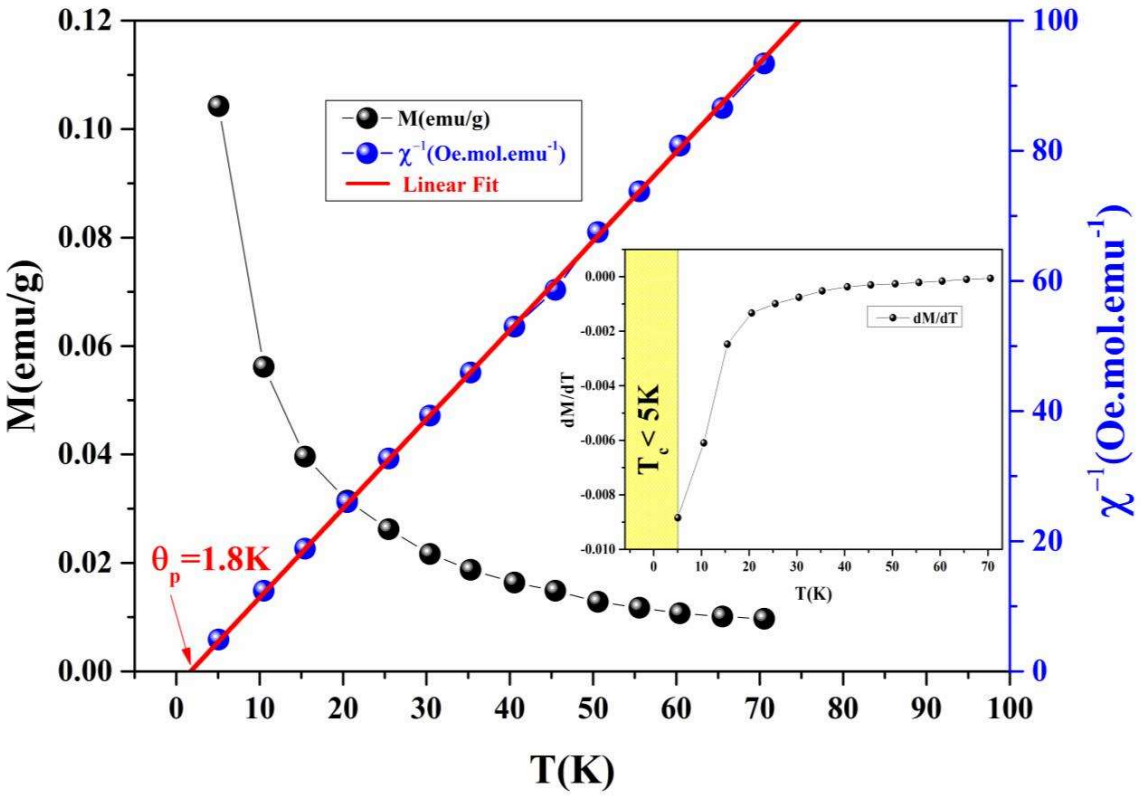
M(emu/g)
χ^{-1}(Oe.mol.emu^{-1})
Linear Fit
θ_p=1.8K
M(emu/g)
χ^{-1}(Oe.mol.emu^{-1})
T(K)
dM/dT
T_c < 5K
dM/dT
T(K)

Fig.12

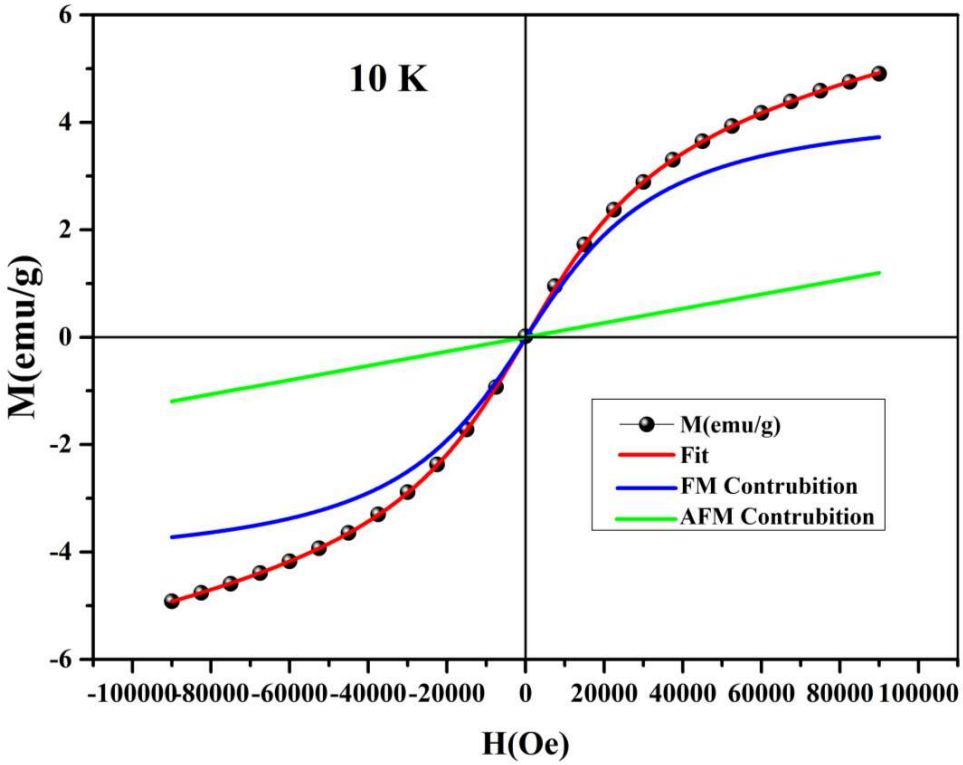
10 K
M(emu/g)
H(Oe)
M(emu/g)
Fit
FM Contrubition
AFM Contrubition

Fig.13

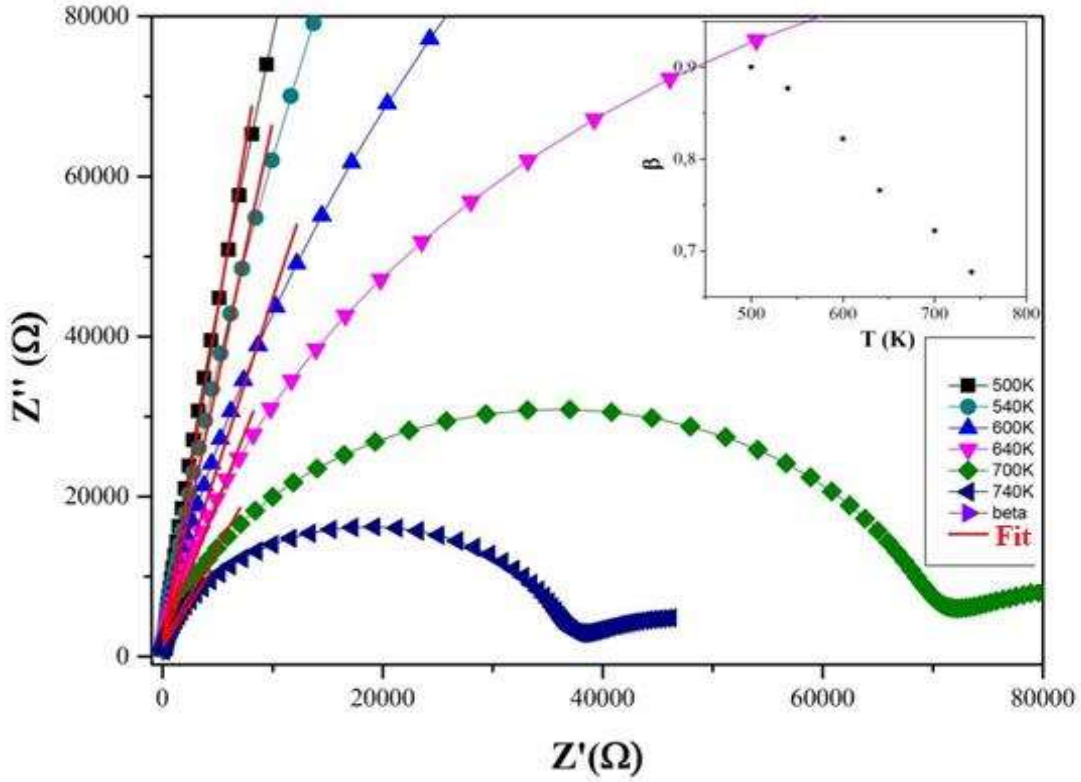
Z'' (Ω)
Z'(Ω)
β
T (K)
500K
540K
600K
640K
700K
740K
beta
Fit

Fig 14

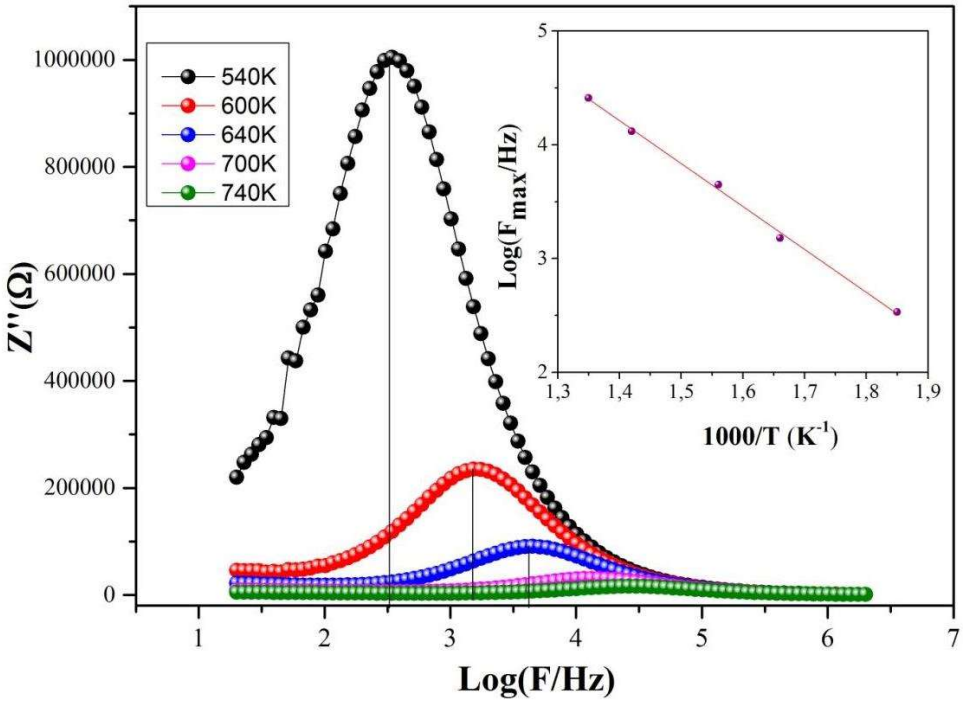
540K
600K
640K
700K
740K
Z''(Ω)
Log(F/Hz)
Log(F_max/Hz)
1000/T (K^-1)

Fig 15

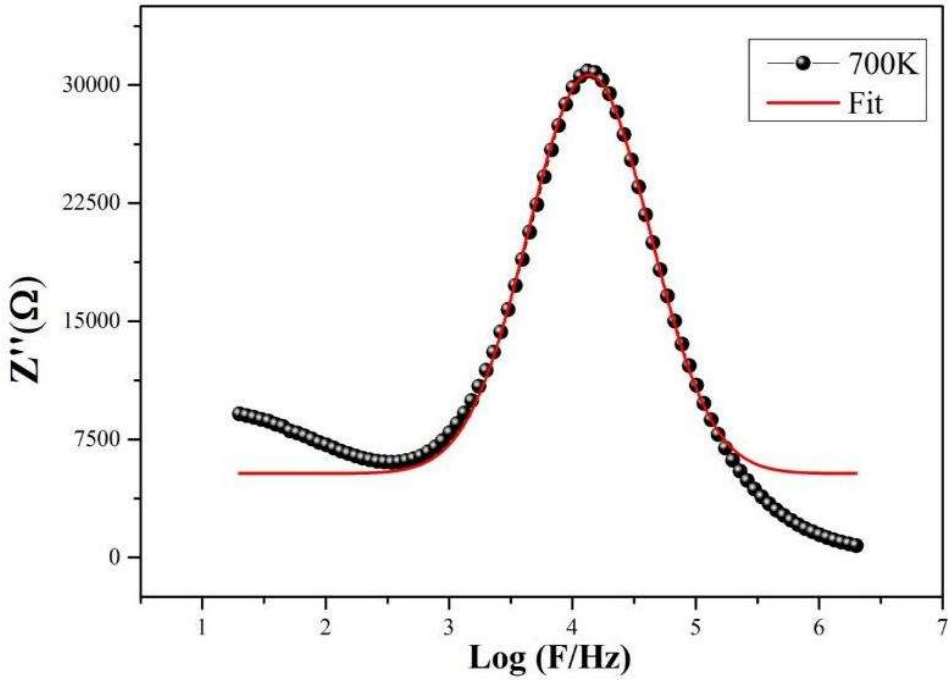
700K
Fit
Z''(Ω)
Log (F/Hz)

Fig 16

Captions Table

Table 1: Experimental condition and crystal structure data of $ZrTe_3O_8$:2%Er, 3%Mn.

Table 2: Equivalent positions and isotropic thermal parameters of $ZrTe_3O_8$:2%Er, 3%Mn.

Table 3: The lattice parameters and the bond distance for both $ZrTe_3O_8$ and $ZrTe_3O_8$:2%Er, 3%Mn.

Table 4: Magnetic characteristics of the $ZrTe_3O_8$:2%Er 3%Mn.

Table 1

Formula	**$ZrTe_3O_8$:2%Er,3%Mn**
Temperature (K)	273
a(Å)	11.3160_1
Space group	Ia-3
V(Å^3)	1449.188_5
Z	8
Diffractometer	Burker D8
Radiation(Å)	Cu $K_{\alpha 1}$ (1.5406)
2θ Range of refinement(°)	19.8795- 79.8846
R_P	18
R_{wp}	21.5
R_{exp}	12.47
R_F	3.67
R_{Bragg}	5.40
χ^2	2.96

Table 2

Atoms	**Site**	**x**	**y**	**z**
Te	24d	0.00	0.25	0.044
Zr	8a	0.25	0.25	0.25
Mn	8a	0.25	0.25	0.25
Er	8a	0.25	0.25	0.25
O1	16c	0.076	0.076	0.076
O2	48e	0.109	0.312	0.149

Table 3

	$ZrTe_3O_8$	$ZrTe_3O_8$:2%Er, 3%Mn
Space group	I a-3	I a-3
a(Å)	11.308_1	11.3160
$\mathbf{d_{Te\text{-}O1}}$	2.166_7	2.17794_{10}
$\mathbf{d_{Te\text{-}O2}}$	1.858_2	1.86165_6
$\mathbf{d_{Zr\text{-}O2}}$	2.073_2	2.07405_7

Table 4

Curie-Weiss Fit Parameters					
C(emu.K.mol^{-1}.Oe^{-1})		**Tc(K)**	$\boldsymbol{\theta p(K)}$	$\boldsymbol{\mu_{eff}^{the}\ (\mu_B)}$	$\boldsymbol{\mu_{eff}^{exp}(\mu_B)}$
0.730		< 5	1.8	1.512	2.417
Hysteresis Fit parameters					
FM			**%FM**	**%AFM**	**Msat(emu/g)**
$\boldsymbol{M_{FM}^R(emu/g)}$	***Hc(Oe)***	$\boldsymbol{M_{FM}^S(emu/g)}$	$\boldsymbol{\chi\ (10^{-5})}$		
0.01583	141	4.659	75.6651	24.335	4.9199